Fractional quantum Hall interface induced by geometric singularity

Qi Li [1,2,*,†] Yi Yang [3,*] Zhou Li,[1,2,4] Hao Wang,[5] and Zi-Xiang Hu [3,‡]

[1]*GBA Branch of Aerospace Information Research Institute, Chinese Academy of Sciences, Guangzhou 510700, People's Republic of China*
[2]*Guangdong Provincial Key Laboratory of Terahertz Quantum Electromagnetics, Guangzhou 510700, People's Republic of China*
[3]*Department of Physics and Chongqing Key Laboratory for Strongly Coupled Physics, Chongqing University,*
Chongqing 401331, People's Republic of China
[4]*University of Chinese Academy of Sciences, Beijing 100039, People's Republic of China*
[5]*Shenzhen Institute for Quantum Science and Engineering, Southern University of Science and Technology,*
Shenzhen 518055, People's Republic of China

The geometric response, which goes beyond the electromagnetic response, of quantum Hall (QH) liquids is crucial for understanding their topological characteristics. According to the Wen-Zee theory, the topological spin is intricately linked to the curvature of the space in which the electrons exist. The presence of conical geometry offers a local, isolated geometric singularity, making it an ideal setting for exploring geometric responses. In the context of two-dimensional electrons in a perpendicular magnetic field, each Landau orbit occupies the same area. The cone geometry naturally provides a structure where the distances between adjacent orbits vary gradually and can be easily adjusted by modifying the tip angle. The cone tip introduces a geometric singularity that impacts electron density and interacts with electron motion, which has been extensively studied. Additionally, this geometry automatically creates a smooth interface or crossover between the crystalline charge-density-wave state and the liquidlike fractional QH state. In this paper, we investigate the properties of this interface from multiple perspectives, shedding light on the behavior of QH liquids in such geometric configurations.

I. INTRODUCTION

Fractional quantum Hall (FQH) effects have revealed a range of exotic topologically ordered phases since their discovery [1] more than three decades ago. As an emergent phenomenon arisen from the two-dimensional electron system interacting with the perpendicular magnetic field, numerous theoretical and experimental investigations are devoted to it. A seminal work is contributed by Laughlin [2], who gave an elegant trial wave function describing a partial filling $\nu = \frac{1}{3}$ state in the lowest Landau level (LLL), which was proven to have fractional excitation and statistics. More exotic FQH states, such as the Moore-Read (MR)-like state at half-filling in the first Landau level with $\nu = \frac{5}{2}$, have been found to host non-Abelian topological excitations and statistics [3,4]. In addition to the regular descriptions of a quantum Hall (QH) system from the electromagnetic response, the topological state also has a response to the geometric manifold where the electrons live. For example, the FQH state on a torus has topological degeneracy, and that on a sphere has a topological shift. The geometric responses including the anomalous viscosity [5–7] and the gravitational anomaly [8–10] are less well known but are topological characteristics of the QH state. Haldane [11] and Park and Haldane [12] pointed out that the internal

geometrical degree of freedom to the variation of the correlation hole shape is responsible for the dynamical variation of the guiding-center metric. Following seminal work by Wen and Zee [13], more efforts have been devoted to the response of FQH states to changes in spatial geometry and topology, such as points of singular curvature in real space or geometry with different genus [14–16].

Recently, experimental efforts have been devoted to creating synthetic materials in artificial magnetic fields such as cold atoms and photonic systems [17–25]. Ultracold atomic gases in a fast rotating trap could be employed to the study of QH phases and transitions, as one can precisely control the dipole-dipole interaction in an anisotropic way [26–34]. Likewise, artificial gauge fields could also be generated for photons. The Landau levels and even Laughlin-type FQH state for photons have been actualized [35–40]. In experiment [38–40], photons have been confined in a plane with several copies. Each copy is confined in a conical geometry. It not only provides the trap stability against the centrifugal limit but also constructs pointlike curved space with nonzero curvature at the tip. The gravitational anomaly has already been extracted from the particle density near the cone tip with coupling to the local curvature [14,16]. Three topological quantities—Chern number, mean orbital spin, and chiral central charge—have been measured through local electromagnetic and gravitational responses [39]. Due to the holomophism feature of the FQH wave function, the radial direction length of a cone manifold extends gradually accompanied by decreasing the cone angle, namely, increasing the number of copies in the experiment. The

————
*These authors contributed equally to this paper.
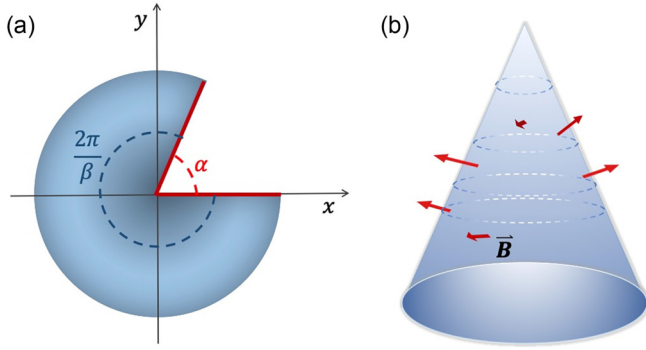†liqi@aircas.ac.cn
‡zxhu@cqu.edu.cn

FIG. 1. The sketch of a cone built from a planar disk. (a) The cone mapped to a plane with deficit angle α and the remaining part with angle $\frac{2\pi}{\beta} = 2\pi - \alpha$. (b) The three-dimensional perspective of a cone with a uniform magnetic field $\vec{B}$ penetrating the surface, and single-particle orbitals are formed with symmetric gauge on a cone.

interval between two adjacent Landau orbits is thus increased and less overlapped. In this geometry, the change rate of the intervals is inhomogeneous since each Landau orbit occupies a fixed area $2\pi l_B^2$. Therefore, the Landau orbits near the tip are far apart from each other compared with that near the edge. Like the Tao-Thouless (TT) state formed in the cylinder geometry, the electrons tend to form a crystalline TT state in the thin cylinder limit. Because of the inhomogeneous change rate of the intervals of Landau orbits, the TT state is first formed near the cone tip and thus a smooth interface, or a crossover naturally emerges in the bulk separating the crystalline phase and the FQH phase without artificial cut-and-glue operations [41] or designing double-quantum-well systems [42].

In this paper, we investigate several properties of FQH states on a cone with the help of Jack polynomials and Monte Carlo (MC) simulation [43,44]. The rest of this paper is arranged as follows. In Sec. II, we briefly introduce the single-particle eigenstates on cones. The ground-state wave function of the many-body Hamiltonian of FQH systems could be obtained numerically using exact diagonalization (ED) or the Jack polynomials method. Section III gives the density profile and charge distribution for two typical FQH states on cones. We calculate the orbital angular momentum which agrees well with the theoretical predictions, revealing the gravitational anomaly coming from the curvature singularity. In addition, the low-lying spectrum shows opposite chirality near the induced interface compared with disk geometry. We perform calculations with respect to wave function overlap and pair correlation functions based on conical wave function profiles in Sec. IV. Furthermore, we investigate the entanglement entropy in momentum space to record the formation of the interface and manipulate the bipartition of the system in real space with an exact cutting position which could efficiently experience the singular curvature in real space. Conclusions and discussion are presented in Sec. V. Some technical details of MC simulation are given in the Appendixes.

II. MODEL AND METHOD

As illustrated in Fig. 1, the creation of an isolated point with singular spatial curvature can be achieved by excising

a sector with a specific apical angle from a disk and subsequently joining the resulting edges. This leads to the formation of a cone-shaped geometry that features a point of singular curvature at its tip, making it an ideal platform for physical studies. Experimental creation of such points within lattice systems is feasible. Notably, the curvature of a cone exhibits singularity solely at its tip in the Gaussian curvature field, vanishing elsewhere [9,13,15,45]. The Gauss-Bonnet theorem ensures that the integrated curvature encompassing the apex of the cone is connected to the deficit angle α:

$$\int K(r)dS = \alpha = 2\pi\left(1 - \frac{1}{\beta}\right). \quad (1)$$

The two-dimensional charge carriers on the surface of a cone which is penetrated by uniform magnetic field $\vec{B}$ have effective single-particle Hamiltonian:

$$H_0 = \frac{1}{2m}(\mathbf{P} + e\mathbf{A})^2. \quad (2)$$

In the symmetric gauge $\mathbf{A} = \frac{B}{2}(-y, x)$, one can express the eigenstate wave function of the Hamiltonian H_0 in a manner like that in disk geometry. Typically, there are two types of single-particle wave functions [46], and the type-I wave function can be formulated as follows:

$$\Phi_{n,m}^I(z) = \mathcal{N}_{n,m} z^{\beta m} L_n^{\beta m}\left(\frac{|z|^2}{2}\right) \exp\left(-\frac{|z|^2}{4}\right), \quad (3)$$

where the complex coordinate $z = (x + iy)/\ell_B = |z|e^{i\theta}$, with $\arg(z) = \theta \in [0, 2\pi/\beta]$. We set the magnetic length $\ell_B = \sqrt{\hbar c/eB} = 1$. Here, $L_n^{\beta m}(|z|^2/2)$ is a generalized Laguerrel polynomial. Here, we can separate the angular and radial variations of the eigenstate wave function into distinct components:

$$\Phi(|z|, \theta) = \phi(|z|) \exp(i\beta m\theta), \quad (4)$$

and the periodic boundary condition $\Phi(|z|, 2\pi/\beta) = \Phi(|z|, 0)$ comes from the joining operation. The corresponding type-I eigenvalues:

$$E_{n,m}^I = \left(n + \frac{1}{2}\right)\hbar\omega_c, \quad (5)$$

with $n, m = 0, 1, 2, \ldots$, are independent of m and responsible for the macroscopic degeneracy of the LLs. The type-II eigenstates:

$$\Phi_{n,m}^{II}(z) = \mathcal{N}_{n,m} z^{*\beta m} L_n^{\beta m}\left(\frac{|z|^2}{2}\right) \exp\left(-\frac{|z|^2}{4}\right), \quad (6)$$

have eigenvalues

$$E_{n,m}^{II} = \left(n + \beta m + \frac{1}{2}\right)\hbar\omega_c, \quad (7)$$

with $n = 0, 1, 2, \ldots$ and $m = 1, 2, \ldots$, which are related to m and β. The normalization factor is

$$\mathcal{N}_{n,m}^2 = \frac{\beta n!}{2\pi 2^{\beta m}\Gamma(n + \beta m + 1)}. \quad (8)$$

When parameter $\beta = 1$, i.e., the flat disk case, the LL index for type-I states is given by $n_{LL} = n$, but $n_{LL} = n + m$ for type-II states, and both cases are degenerate. When parameter $\beta > 1$, i.e., a general cone case, type-I states remain unchanged, while energies of type-II states elevate to the

internal levels inside the inter-LL gaps. The states in the LLL come from type I with energy $E = \frac{1}{2}\hbar\omega_c$, and we will use the single-particle wave function, which refers to type-I $\Phi_{0LL} = \mathcal{N}_{0,m}z^{\beta m}\exp(-|z|^2/4)$ in subsequent parts with no superscript.

The Laughlin state at $\nu = \frac{1}{3}$ can be obtained by diagonalizing the hard-core model Hamiltonian with Haldane's pseudopotential V_1 [2,47]. The low-lying energy spectra are obtained using the ED method. It is known that the model wave functions could also be obtained with the help of a Jack polynomial which is characterized by a root configuration and a parameter α [48–50]. For example, the root configuration for the Laughlin state is $1001001\cdots$ and $11001100\cdots$ for the MR state [4]. The leftmost orbit represents the innermost Landau orbit which could be the center of a flat disk or the cone tip. In addition to the ground state, one can similarly describe quasihole states with one addition unoccupied orbit at the cone tip, namely, $01001001\cdots$. In general, it is straightforward to consider Laughlin's model wave function $\Psi_L(z_1,\ldots,z_N) = \prod_{j<k}(z_j-z_k)^m e^{-(1/4)\sum_i |z_i|^2}$ for a state with a single quasihole located at z_0, $\Psi_{qh}(z_0) = \prod_i(z_i-z_0)\Psi_L(z_1,\ldots,z_N)$. Based on these model wave functions obtained from Jack constructions, we calculate the density profile, accumulated charge, overlap, pair correlation functions, and entanglement properties. In addition, it is convenient to use the Metropolis MC method to get the mean orbital occupation number $\langle n \rangle$ for larger system size such as 20 electrons for the Laughlin and MR states, the orbital angular momentum with 50 electrons, and the edge Green's function with 30 electrons.

III. CHARGE DENSITY PROFILES

The incompressible topological FQH ground state exhibits a uniform bulk density $\rho_0 = \nu/2\pi\ell_B^2$ at a filling factor ν in a smooth space, such as an infinite plane. However, in the presence of a QH edge or interface, the density becomes nonuniform. Furthermore, in a curved space, there is an additional correction to the density that takes the following form:

$$\rho = \frac{\nu}{2\pi\ell_B^2} + \frac{\nu K(r)}{8\pi}(\mathcal{S} - 2j), \tag{9}$$

with the Gaussian curvature $K(r)$, the particle spin j [51], and the topological shift $\mathcal{S}$ [13]. The topological shift $\mathcal{S} = \nu^{-1}$ for the fermionic Laughlin state and $\mathcal{S} = \nu^{-1} + 1$ for the fermionic MR state. In spherical geometry, the curvature is uniform, resulting in a constant correction everywhere, and thus, the charge density remains uniform. Conversely, in conical geometry, nonzero curvature emerges at the apex, leading to an excess charge density at the apex of the cone. This difference in curvature between spherical and conical geometries causes variations in charge density in the corresponding systems. Figure 2(a) displays the radial density profile for a 10-electron $\nu = \frac{1}{3}$ Laughlin state, with $\beta \in [1, 10]$. Here, $\beta = 1$ corresponds to a plane disk with no curvature, and thus, the density at the apex equals the bulk density value $2\pi\rho(r) = \nu$. When $\beta > 1$, there is charge accumulation around the cone apex, as observed in the bosonic FQH state [16]. It is worth noting that, as β increases, the density profile approaches β at the cone tip. Explicitly, the cone tip density $\rho(0) = \sum_m |\Phi_m(0)|^2\langle\Psi_0|C_m^\dagger C_m|\Psi_0\rangle = \frac{\beta}{2\pi}\langle\Psi_0|C_0^\dagger C_0|\Psi_0\rangle \to \frac{\beta}{2\pi}$. This
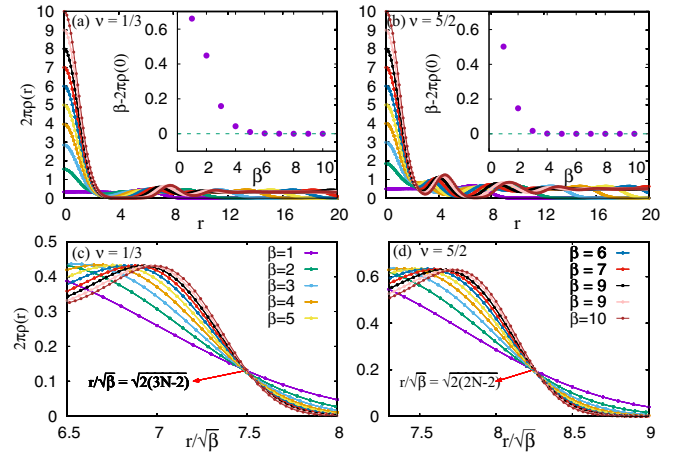

FIG. 2. The density profile $2\pi\rho(r)$ as a function of r for (a) the $\nu = \frac{1}{3}$ Laughlin state and (b) the $\nu = \frac{5}{2}$ Moore-Read (MR) state on cones. The inset plots in (a) and (b) show $\beta - 2\pi\rho(0)$ vs β with respect to the corresponding states, respectively. (c) and (d) Zoom-ins of the density profile near the physical edge $r = \sqrt{2N_{orb}\beta}$ in rescaled coordinate axis $r/\sqrt{\beta}$. The system size for (a) and (c) the Laughlin state is 10 electrons and for (b) and (d) the MR state is 18 electrons.

suggests that the zeroth orbital is fully occupied, leading to a crystalline state at the apex. For the Laughlin state, it is shown that the condition for this behavior is $\beta > 4$, as indicated in the inserted figure, which plots $\beta - 2\pi\rho(0)$ vs β.

On the contrary, as β increases, the surface area for a fixed radius decreases, as illustrated in Fig. 1. This results in radial stretching of the cone while maintaining the total area unchanged. Consequently, as β rises, the edge moves away from the apex point, making it easier for the system to establish a universal QH edge. The density profiles near the edge exhibit a crossover behavior with a rescaled radius $r/\sqrt{\beta}$, as shown in Fig. 2(c). The crossover point is located at $r/\sqrt{\beta} = \sqrt{2N_{orb}} = \sqrt{2(3N - 2)}$, which corresponds to the physical edge for the N-electron Laughlin state in $(3N - 2)$ orbits. In Figs. 2(b) and 2(d), we present similar data for the MR state, another intriguing trial state for the $\nu = \frac{5}{2}$ FQH liquid that is conjectured to possess non-Abelian topological order. Like the Laughlin state, an excess density profile persists at the cone tip with an exact value of $2\pi\rho(0) = \beta$ when $\beta > 3$. The density exhibits a crossover at its physical edge $r/\sqrt{\beta} = \sqrt{2(2N - 2)}$. Moreover, the density at the cone tip exhibits more pronounced oscillations than that of the Laughlin state, indicating different geometric responses for different FQH states.

To obtain more detailed information about the charge distribution, we can calculate the accumulated charge over an area that encloses the cone tip in real space:

$$Q(R) = \int_0^R \rho(r)\frac{2\pi r}{\beta}dr. \tag{10}$$

This calculation will enable us to investigate the distribution of charge within the system and determine if there are any localized regions of excess charge density near the cone apex. As shown in Figs. 3(a) and 3(b), as the integrated internal $[0, R]$ increases, the accumulated charge Q starts from zero and increases to the total number of electrons N in the system.
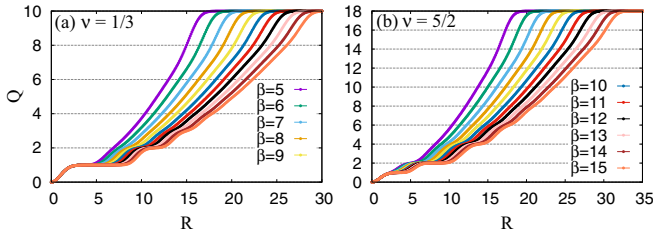
FIG. 3. The quantity Q in Eq. (10) as a function of the upper limit R of integration for (a) the $\nu = \frac{1}{3}$ Laughlin state and (b) the $\nu = \frac{5}{2}$ Moore-Read (MR) state on cones. The system size for the Laughlin state is 10 electrons and for the MR state is 18 electrons.

As we know, a larger β makes the cone thinner and stretches the distance between the two nearest electrons, like the case of a thin cylinder. As a result, it becomes easier to count the charges as the enclosed integrated area gradually grows. However, unlike the disk case with a smooth ascending curve, step plateaus emerge starting from the cone tip for large β cases, indicating the formation of charge-density-wave (CDW) patterns. In analogy to disk geometry with symmetric gauge, the Landau orbits on cones are not uniformly distributed, so the charge plateaus in real space show different lengths. Furthermore, we notice that the integrated charge step is not always one for the MR state. The first ladder jumps by only one electron charge, but the following ladders jump by two electron charges. The contributions from the paired ground-state root configuration approximately explain the two-step jumping, and the one-step jumping could be attributed to the curvature singularity at the cone tip, which always captures one electron if β is large enough. However, in the $\beta \to \infty$ limit, the ladder jumping steps will always be one with two jumps located closer together as a group (11), and the plateaus between two groups will take longer intervals (00). The charge pattern can be observed more clearly through the mean orbital electron occupation number $\langle c_n^\dagger c_n \rangle = \langle n \rangle$. For large system sizes, the occupation numbers can be evaluated using the MC method [43,52,53] with the aid of the one-particle reduced density matrix [54]. The technical details for cone geometry are discussed in Appendixes A and B. As β increases, Fig. 4 illustrates the emergence of an interface that separates the droplets into two distinct regions. In the region close to the cone tip, a CDW (TT) phase begins to form, with the leftmost orbital always being occupied. In contrast, the region near the other end of the cone preserves the FQH states.

A. Orbital angular momentum (OAM)

The net moment of the cone tip should be captured to determine the OAM of the cone tip. This can be achieved by carefully analyzing the spatial distribution of the electron density profile at the cone tip. The net moment can then be calculated as follows:

$$L_{\text{tip}} = \int \left(\frac{r^2}{2} - 1 \right) \Delta\rho(r) dS, \quad (11)$$

where $\Delta\rho(r) = \rho(r) - \nu/(2\pi)$. The presence of a singularity at the origin in the cone geometry indeed leads to the existence of a net momentum. This net momentum is a result of the
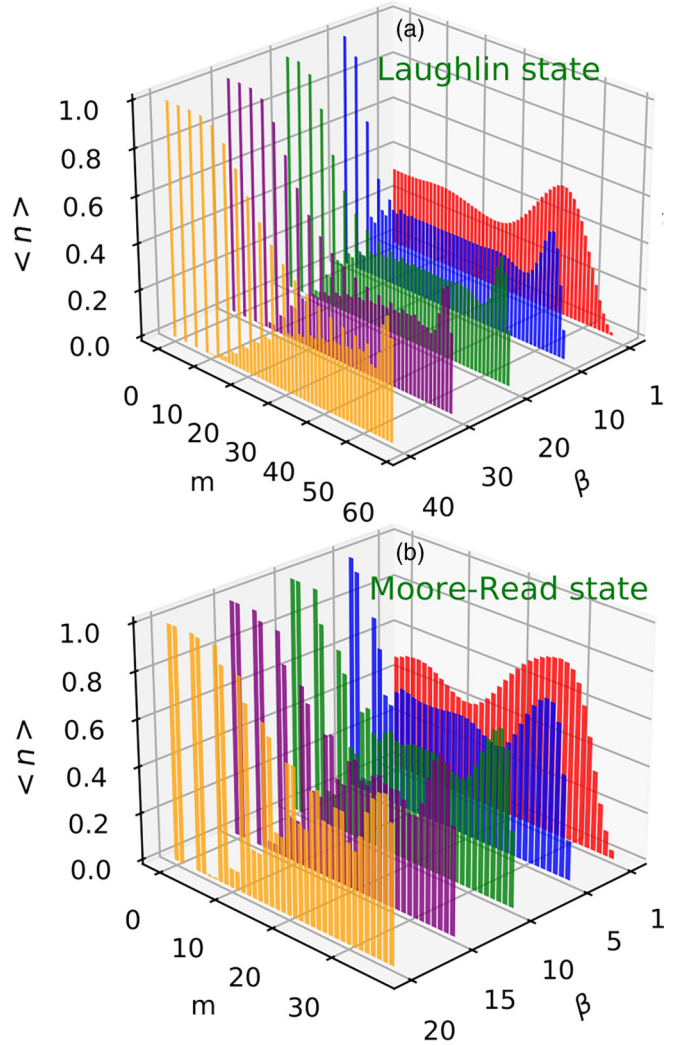

FIG. 4. The mean orbital occupation number $\langle n \rangle$ for (a) the Laughlin state and (b) the Moore-Read (MR) state with 20 electrons on cones. In each case, five discrete β values are considered.

gravitational anomaly and is associated with significant topological quantum numbers. However, when the thermodynamic limit is considered, the net momentum vanishes in the disk geometry. The conformal symmetry has the following prediction [9,39]:

$$L_{\text{tip}} = \frac{c - 12\nu\bar{s}^2}{24} \left(\beta - \frac{1}{\beta} \right) + \frac{a}{2} \left(2\bar{s} - \frac{a}{\beta} \right), \quad (12)$$

where c is the chiral central charge and $\bar{s}$ is the mean orbital spin of conformal field theory. Here, a is the excess flux quanta through the cone tip which could take three values $0, \frac{1}{3}, \frac{2}{3}$. Here, we note that the central charge c_H of Ref. [9] and c of Ref. [39] are related by $c_H = c - 12\nu\bar{s}^2$. Therefore, if we consider a Laughlin state at $\nu = \frac{1}{3}, \bar{s} = \nu^{-1}/2, c = 1$ and $c_H = -8$. In the above formula, the first term is brought by the conical tip defect, while the second term is related to quasihole with charge e/ν. Here, we consider FQH states without any extra flux threading at the cone tip; in other words, $a = 0$. In
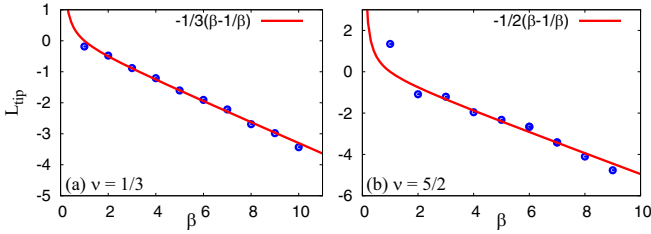
FIG. 5. The orbital angular momentum (OAM) of the cone tip for (a) the $\frac{1}{3}$ Laughlin state and (b) the Moore-Read (MR) state. The line is the theoretical value which is described as $L_{tip} = \frac{c - 12\nu\bar{s}^2}{24}(\beta - \frac{1}{\beta}) + \frac{a}{2}(2\bar{s} - \frac{a}{\beta})$, with $c = 1$, $\bar{s} = \frac{1}{2}\nu^{-1}$, and $a = 0$ for the $\frac{1}{3}$ Laughlin state and $c = 3/2$, $\bar{s} = \frac{3}{2}$, and $a = 0$ for the MR state.

this case, OAM is reduced to

$$L_{tip} = \frac{c - 12\nu\bar{s}^2}{24}\left(\beta - \frac{1}{\beta}\right). \tag{13}$$

In our numerical analysis, we have accurately determined the value of L_{tip} for both the Laughlin and MR states through MC simulations of a large system containing up to 50 electrons. To achieve this, we employed an integral upper bound denoted as R, which was situated well away from both the cone tip and the edge of the system. The results of our calculations are presented in Fig. 5, which clearly illustrates a linear relationship between L_{tip} and $\beta - \frac{1}{\beta}$. Notably, the fitting slope obtained from our numerical data aligns well with the theoretical predictions, highlighting the accuracy of our findings.

In the subsequent analysis, we will delve into the characteristics of the low-lying excitations in the system. To illustrate this, we will use the Laughlin state as a case study, which is defined by a model Hamiltonian that incorporates a hard-core interaction. Notably, in this model, only the Haldane's pseudopotential V_1 assumes a nonzero value. In a system containing 10 electrons in 28 orbitals, we will explore the energy spectrum at various values of β, as displayed in Fig. 6.
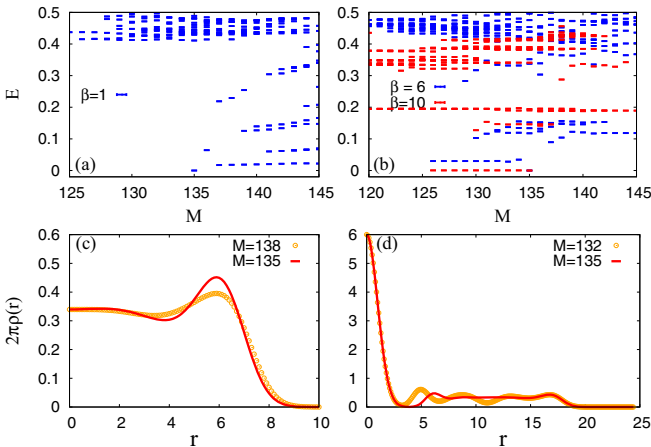

FIG. 6. The low-lying energy spectrum of a Hard-core interaction with different (a) $\beta = 1$ and (b) $\beta = 6, 10$. The density profile comparison between the Laughlin state and one of the excited states is depicted in (c) and (d).

The ground state of this system is marked by a total angular momentum $M_{tot} = M_0 = 3N(N-1)/2 = 135$, which corresponds to zero energy. By exploring the energy spectrum across various β values, we can gain deeper insights into the behavior of the system and the nature of its low-lying excitations.

In the case of the plane disk with $\beta = 1$, the lowest excited states are the chiral edge excitations, which possess a total angular momentum M_{tot} greater than the ground-state angular momentum M_0. However, as β increases, these states are gradually lifted in energy, and energy levels with $M_{tot} < M_0$ are suppressed. This leads to the evolution of these suppressed energy levels into the lowest excited states for $\beta > 5$. Interesting, this is exactly the criterion for the development of the interface, as discussed previously in Fig. 2(a). In Fig. 6(b), we observe that, for $\beta = 6$, nearly degenerate energy levels in the range $M_{tot} \in [126, 134]$ emerge as the low-lying excitation branch. This behavior reflects the influence of β on the energy spectrum and the emergence of new low-lying excitations in the system. Figures 6(c) and 6(d) compare the radial density between the ground state $M_0 = 135$ and one of the lowest excited states at $M_0 \pm 3$. Obviously, for $\beta = 1$, the $M = 138$ state is indeed an edge excitation, exhibiting a density perturbation near the edge. Conversely, for $\beta = 6$, the $M = 132$ state exhibits a density perturbation in the bulk while maintaining a constant density at the cone tip and edge. This can be explained as an interface excitation, which possesses a lower energy than the edge excitation. It is worth noting that, as β increases further, the excitation energy branch of the interface continues to be suppressed and eventually becomes a zero-energy branch, as shown in Fig. 6(b).

IV. WAVE FUNCTION PROFILES

Intuitively, for large enough β, the cone is extremely stretched and resembles the thin cylinder [55–57] limit. To specify the continued transition to the CDW TT state [58], we describe the overlap between wave functions on a cone with varying β and that on a cylinder with varying the circumference L_y (or equivalent L_x) for the same system size. In Fig. 7, we plot the corresponding overlaps $|\langle\Psi_{cone}(\beta)|\Psi_{cylinder}(L_x)\rangle|$ for both the Laughlin and MR states. When it comes to the cylinder, we understand that it solely represents an incompressible fluid under specific conditions. Specifically, when the lengths L_y and L_x of the cylinder are comparable, and as L_y approaches zero or L_y tends toward infinity, the ground state assumes the form of a gapped crystal known as the TT state. In our numerical tests, as illustrated in Fig. 7(a), the overlap between the ground state on the cylinder and the CDW states approaches unity when $L_x \approx 40\ell_B$ for finite systems. Moreover, in Fig. 7(b), we observe that the wave function overlaps between cones and cylinders asymptotically approach unity, despite the finite values of β. As β approaches infinity, the extrapolation of the positions of the overlap peaks approaches $41.1\ell_B$ with an overlap of 99.3% for the Laughlin state and $34.2\ell_B$ with an overlap of 92.6% for the MR state. It should be noted that the calculation is performed in a finite system, and the extrapolation of $L_x \simeq 41.1\ell_B$ with $\beta \to \infty$ is not valid in the thermodynamic limit. The aspect ratio $\gamma = L_x/L_y$ would be more appropriate which suffers less of a finite-size effect.
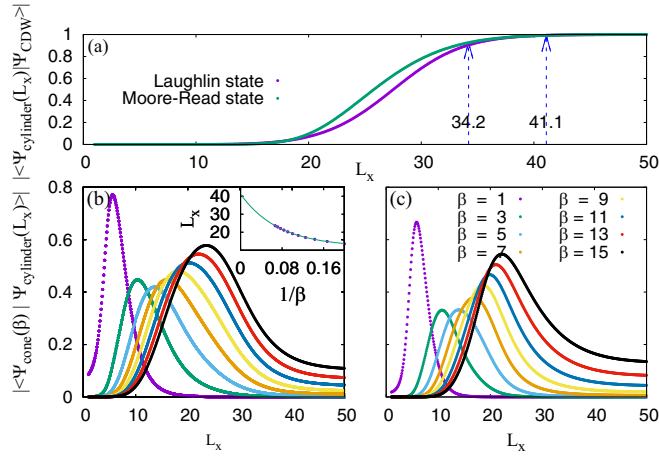
FIG. 7. (a) The overlaps between wave functions on cylinders $|\Psi_{\text{cylinder}}(L_x)\rangle$ and the charge-density-wave (CDW) state as a function of the length L_x. Both the Laughlin and Moore-Read (MR) states are considered. The overlaps $|\langle \Psi_{\text{cone}}(\beta)|\Psi_{\text{cylinder}}(L_x)\rangle|$ between wave functions on cones $|\Psi_{\text{cone}}(\beta)\rangle$ and wave functions on cylinders $|\Psi_{\text{cylinder}}(L_x)\rangle$ are plotted in for (b) the Laughlin state with 10 electrons and (c) the MR state with 16 electrons. The inset plot in (b) gives the extrapolation of the overlap peak positions L_x for large β cases of the Laughlin state, and the fitting function reads $L_x = 29.3371e^{-13.6515/\beta} + 11.973$. The corresponding L_x in $\beta \to \infty$ limit is $\sim 41.1\ell_B$ for the Laughlin state and $34.2\ell_B$ for the MR state, indicated by arrows in (a).

Nevertheless, these findings validate that the limit of $\beta \to \infty$ corresponds to that of a thin cylinder, thus confirming that the state indeed corresponds to the TT state.

A. Pair correlation function

To investigate the evolution of the electron density near the cone tip, we consider the two-point pair correlation function which is defined as

$$g(\vec{r}) = \frac{L_x L_y}{N(N-1)} \langle \Psi| \sum_{i \neq j} \delta(\vec{r} + \vec{r}_i - \vec{r}_j)|\Psi\rangle. \quad (14)$$

While the coordinate of one particle is fixed at the tip, the pair correlation function can be written in a second quantized form as

$$g(r) = \frac{1}{\rho(0)\rho(r)} \sum_{m_i} \Phi^*_{\beta m_1}(r)\Phi^*_{\beta m_2}(0)$$
$$\times \Phi_{\beta m_3}(0)\Phi_{\beta m_4}(r)\langle c^\dagger_{m_1} c^\dagger_{m_2} c_{m_3} c_{m_4}\rangle. \quad (15)$$

It can be obtained using the wave function from either diagonalization or MC simulation [59]. The results are shown in Fig. 8 for both the Laughlin and MR states in the rescaled radial distance. In both cases, $g(r)$ evolves into a sharp step shape. Taking the Laughlin state as an example, the pair correlation function $g(r)$ in a plane disk ($\beta = 1$) exhibits oscillations, characteristic of a liquidlike state. These oscillations are gradually suppressed as the value of β is increased. The peak of $g(r)$, which is >1, disappears at around $\beta = 5$, indicating the formation of a crystalline state near the cone tip, which is consistent with the results from the electron
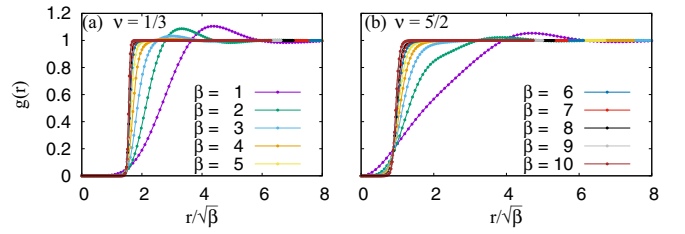

FIG. 8. Pair correlation function $g(r)$ for the $\frac{1}{3}$ Laughlin state and the $\frac{5}{2}$ Moore-Read (MR) state for different β on a cone. The system size for the Laughlin state is 10 electrons and for the MR state is 16 electrons.

density. A similar analysis applies to the MR state as shown in Fig. 8(b).

B. Entanglement

An effective tool to extract topological information from the ground-state wave function of the FQH states is the entanglement spectrum [60], which goes beyond the traditional Landau theory based on symmetry breaking and local order parameters. To be more precise, we consider the bipartite entanglement when the Hilbert space is divided into two parts $\mathcal{H} = \mathcal{H}_A + \mathcal{H}_B$. This partition is characterized by the reduced density matrix $\rho_A = \text{Tr}_B|\Psi_0\rangle\langle\Psi_0|$ after tracing out the degrees of freedom of B. The bipartite operation on ground-state Ψ_0 can be implemented in momentum space [61,62] or alternatively in real space [63,64] of the two-dimensional system. The former is called the orbital cut (OC) and the latter the real-space cut (RC). One can perform Schmidt decomposition on Ψ_0 and express it as $|\Psi_0\rangle = \sum_i \exp(-\xi_i/2)|\psi_i^A\rangle \otimes |\psi_i^B\rangle$, where $|\psi_i^A\rangle$ and $|\psi_i^B\rangle$ are orthonormal bases providing a natural bipartition of the system. The singular values set $\exp(-\xi_i/2)$ reveals the entanglement energies ξ_i, which was introduced by Li and Haldane [60]. As an entanglement measurement, the entanglement entropy is defined associated with ρ_A, i.e., the Von Neumann entropy reads $S_A = -\text{Tr}_A[\rho_A \ln \rho_A]$. For two-dimensional topological systems, the entanglement entropy satisfies the area law with a first correction which is named the topological entanglement entropy γ [65–67]. Here, L is the boundary length between two systems in the two-dimensional case, and α is a nonuniversal number depending on the way of the bipartition $S \simeq \alpha L - \gamma$. As a topological order, $\gamma = \ln \mathcal{D}$ is related to the total quantum dimension $\mathcal{D}$ characterizing the topological field theory associated with the phase and the nature of the system excitations. As we know, the quantum dimension characterizes the growth rate of the Hilbert space with an anyon number, and for the fermionic Laughlin state with anyonic excitations and filling fraction $\nu = 1/m$, it reads $\mathcal{D} = \sqrt{m}$. In addition, when a topological excitation or quasiparticle emerges in the system, we can detect the quantum dimension of the quasiparticle d_α using the additional change of topological entanglement entropy $\gamma^{qp} = \ln \mathcal{D} - \ln d_\alpha$. In general, the quantum dimension $d_\alpha = 1$ for Abelian quasiparticles, but $d_\alpha > 1$ for non-Abelian quasiparticles.

In this paper, we investigate the entanglement entropy of the Laughlin and MR states on cones, both for the OC and
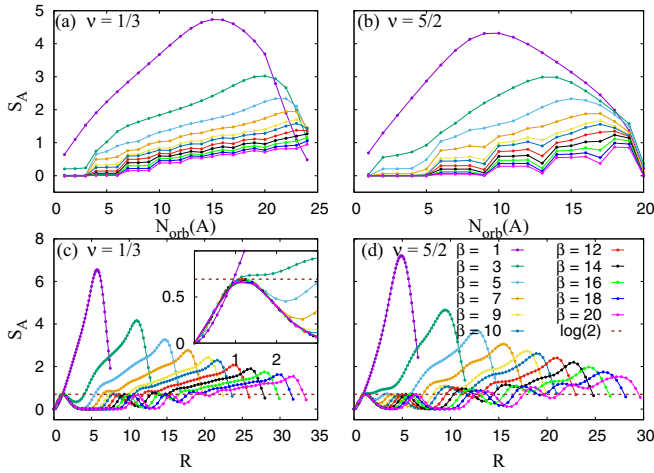
FIG. 9. The orbital cut entanglement entropy S_A as a function of $N_{orb}(A)$ for (a) the Laughlin state and (b) the Moore-Read (MR) state on cones. The total Landau orbital in subsystem A, $N_{orb}(A)$, varies as we cut the system in momentum space in different positions. The real space cut entanglement entropy S_A as a function of cutting position R for (c) the Laughlin state and (d) the MR state on cones. The system size for (a) and (c) the Laughlin state is 10 electrons and for (b) and (d) the MR state is 12 electrons. The inset plot in (c) is the enlarged data S_A for $R \in [0, 3]$. The dashed line is exactly the classical Von Neumann entropy $S = \ln(2)$.

RC cases. Our focus is on the impact of the emergence of a CDW phase on entanglement entropy in both real space and momentum space. For the OC case, it is natural to vary the cutting position by adjusting the number of Landau orbitals in subsystem A, $N_{orb}(A)$. Here, we define the leftmost $N_{orb}(A)$ consecutive orbitals as belonging to part A, corresponding to the inner circle of a disk or the upper part of a cone. Part A maintains the same shape as the entire system but differs in the number of orbitals. We focus on the cone case, particularly when a large singularity affects the tip. As β increases, we observe in Figs. 9(a) and 9(b) that the global entropy S_A monotonically decreases. When $\beta > 4$, entropy S_A approaches zero for $N_{orb}(A) = 1, 2, 3$ in Fig. 9(a). This suggests that the cone tip loses its correlation with the bulk as the crystalline state forms. Interestingly, three consecutive data points form a set with almost identical S_A, creating a steplike structure. For example, in the $\beta = 14$ case, three steps are evident, consistent with the occupation pattern $1001001001\cdots$ in the TT state, where three consecutive orbitals serve as a unit cell. Cutting at the leftmost orbitals with $N_{orb}(A) = 1, 2, 3$ has one common feature: Part A contains one electron. When cutting at $N_{orb}(A) = 4, 5, 6$, part A contains two electrons, leading to a new step. For the MR state in Fig. 9(b), large β induces a CDW phase with a configuration of $11001100110011\cdots$. It is evident that $N_{orb}(A) = 1$ and $N_{orb}(A) = 2$ correspond to different N_A cases, while $N_{orb}(A) = 2, 3, 4$ form a step with almost equal S_A. Two additional steps occur at $N_{orb}(A) = 5$ and $N_{orb}(A) = 6$, with $N_A = 3, 4$ respectively.

For the RC case, by cutting the cone along the loop parallel to the basal circumference in real space, a smaller cone defined as part A and the residual part defined as part B are obtained. The generatrix length R of the smaller cone
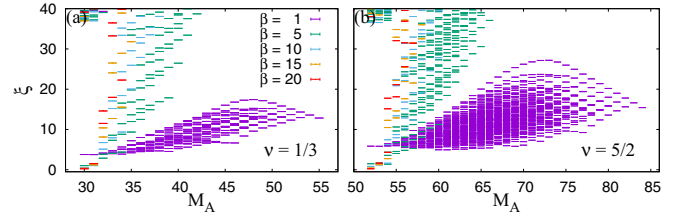

FIG. 10. The orbital cut entanglement spectrum ξ for (a) the Laughlin state and (b) the Moore-Read (MR) state on cones. The system size for the Laughlin state is 10 electrons and for the MR state is 16 electrons.

(part A) is determined by the RC position, and we plot the entanglement entropy S_A against R for the Laughlin and MR states in Figs. 9(c) and 9(d), respectively. First, we notice the figures share a common feature that, near the cone tip, all entropies almost collapse into each other (except the $\beta = 1$ case). The enlarged figure inserted in Fig. 9(c) also shows that, for the cone cases with $\beta > 4$, a first peak occurs around $R = 1.18\ell_B$, with the entropy exactly equal to the classical Von Neumann entropy $S = \ln(2)$. This phenomenon implies that the cutting is right on one electron, and all the patterns for big-enough β cases are almost the same near the cone tip, which again shows consistency for local characteristic length around $1\ell_B$. In addition, with increasing the β value, a second peak will appear with $S_A > \ln(2)$ at larger R and finally equals $\ln(2)$ (cut on electrons again) but never $<\ln(2)$. In the $\beta \to \infty$ limit, there would be $N - 1$ peaks (except the tip one) with values $\ln(2)$, which totally corresponds to the CDW phase and is analogous to the thin cylinder case. However, within the finite β case, the CDW pattern begins from the cone tip side and has an evolution process to fully expand to the whole cone. Compared with the Laughlin state case, the MR state entropy curves in Fig. 9(d) show similar behaviors but with the first two peaks closer. Here, we should note that the first peak occurs also around $R = 1.18\ell_B$. The thinner cone will extend the distance between two neighbor orbitals and lower the correlations or entropy values between two subsystems.

Figure 10 illustrates the entanglement spectrum of the one-cone state for half of the system at different values of β. Notably, the structure of the entanglement spectrum, i.e., the number of states in each momentum space, remains unchanged for all β values. This suggests that increasing β does not lead to a phase transition, indicating that the topological phase of the TT state is the same as that of the Laughlin state. The only variation observed is the steepness of the spectrum. In the TT state, the entanglement is predominantly influenced by the unique ground state in the entanglement spectrum.

C. Edge Green's function

The FQH edge states exhibit a non-Ohmic I-V relation $I \propto V^\eta$ in tunneling experiments, in contrast with the noninteracting Fermi liquid. This behavior can be predicted by chiral Luttinger liquid theory and has been observed in experiments [68]. The parameter η in the I-V relation is a topological quantity of the FQH liquid, with values such as $\eta = 3$ for the $\nu = \frac{1}{3}$ Laughlin state and the MR state, as predicted by chiral Luttinger liquid theory [69,70]. When considering a conical
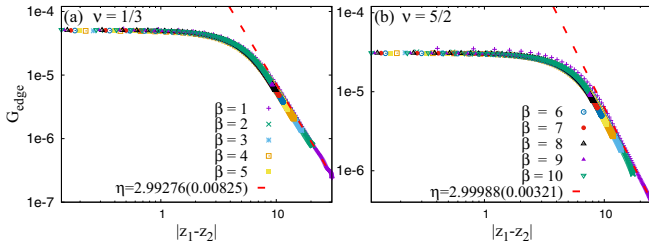
FIG. 11. Edge Green's function for the $\frac{1}{3}$ Laughlin state and the $\frac{5}{2}$ Moore-Read (MR) state for different β with $N = 30$ on a cone. Here, we set $X = 1.9\ell_B$ and $2.13\ell_B$, respectively, for the $\frac{1}{3}$ Laughlin and MR states. The red dashed line is the fitting results.

manifold, the edge of the FQH liquid is located far from the tip where the curvature singularity exists, thereby making the edge physics unaffected by the geometric singularity. Moreover, as the system transitions into the TT state by increasing β, which is topologically equivalent to the Laughlin state, the exponent η should remain constant if it is indeed a topological invariant.

Numerically, the exponent η could be obtained from the equal-time edge Green's function $G_{\text{edge}}(|z_1 - z_2|) \sim |z_1 - z_2|^{-\eta}$. In a system with rotational symmetry, the edge Green's function can be described as

$$G_{\text{edge}}(|\vec{z}_1 - \vec{z}_2|) = \Phi^\dagger(\vec{z}_1)\Phi(\vec{z}_2)$$

$$= \sum_m \frac{\beta}{2\pi 2^{\beta m} \Gamma(\beta m + 1)} z_1^{\beta m} z_2^{\beta m}$$

$$\times \exp[i\beta m(\theta_1 - \theta_2)] \exp\left(-\frac{z_1^2 + z_2^2}{4}\right) n_m,$$

where two points $\vec{z}_1$ and $\vec{z}_2$ are chosen at the edge of a cone, at a distance of $|\vec{z}_1| = |\vec{z}_1| = R = \sqrt{2N_{\text{orb}}\beta} + X$ from the tip, where $\theta = \theta_1 - \theta_2$ is the angle between $\vec{z}_1$ and $\vec{z}_2$, and X is the length of the density tail. Thus, the edge Green's function is rewritten as

$$\Phi^\dagger(\vec{z}_1)\Phi(\vec{z}_2) = \sum_m \frac{\beta}{2\pi 2^{\beta m} \Gamma(\beta m + 1)} R^{2\beta m}$$

$$\times \exp(i\beta m\theta) \exp\left(-\frac{R^2}{2}\right) n_m. \quad (16)$$

Analytically, the chord length between two edge points reads $|\vec{z}_1 - \vec{z}_2| = 2R/\beta \sin(\theta\beta/2)$, with $\theta \in [0, 2\pi/\beta]$.

As depicted in Figs. 11(a) and 11(b), or cones with modified curvature, a perfect fitting exponent $\eta \simeq 3$ for both the Laughlin and MR states while the distance $|z_1 - z_2|$ is large enough, which aligns with the theoretical prediction. Even though a stretched cone has a smaller bottom surface radius, limiting the distance between the two electrons, the edge state of the conical surface still displays the same topological property as the FQH state. The results of the edge Green's function still manifest the topological equivalent between the FQH state and its TT limit.

V. CONCLUSIONS

In summary, our detailed exploration of FQH states on conical manifolds has revealed the emergence of a smooth interface that separates the topologically trivial (TT) state from the FQH liquid. This interface is tunable by gradually adjusting the curvature singularity at the cone tip. The presence of a localized geometric defect at the cone tip results in charge accumulation due to positive curvature, significantly altering the density profile around the apex. The TT state is signaled by the full occupation of the zeroth orbital, while for the Laughlin state, it emerges at $\beta > 4$, and for the MR state, at $\beta > 3$. As the interface between the FQH state and the CDW state forms, the low-energy spectrum is dominated by density oscillations near the interface, rather than edge excitations of the FQH liquid. This observation implies that interface excitations may play a pivotal role in the low-energy physics of realistic scenarios, such as FQH liquids confined in sharp potential wells or experiencing nonuniform electron density. Our OAM calculations align well with theoretical predictions, clearly demonstrating the gravitational anomaly arising from the geometric singularity. However, through careful considerations of wave function overlap, entanglement spectrum, and edge Green's function, we confirm that the FQH state and its TT limit belong to the same topological phase, indicating that the interface in this paper behaves more as a crossover phenomenon.

APPENDIX A: OCCUPATION NUMBER OF $\frac{1}{3}$ LAUGHLIN STATE FROM MC SIMULATION

In this Appendix, we use Metropolis MC simulation to get the occupation number of FQH states on a cone. Comparing the single-particle wave functions in Eq. (3) on cone and disk, the (unnormalized) wave function corresponding to the $\frac{1}{3}$ Laughlin state $|\Psi_{1/3}\rangle$ is

$$|\Psi_{1/3}\rangle = \prod_{j<k} \left(\vec{z}_j^{\,\beta} - \vec{z}_k^{\,\beta}\right)^3 \exp\left(-\frac{1}{4}\sum_i z_i^2\right), \quad (A1)$$

where $\vec{z}_j = x_j + iy_j = z_j \exp(i\theta_j)$ is the coordinate of the jth particle, $\theta_j \in [0, \frac{2\pi}{\beta}]$.

The occupation number of the mth single-particle orbit of $|\Psi_{1/3}\rangle$ is

$$
n_m^{1/3} = \frac{\langle \Psi_{1/3}|c_m^\dagger c_m|\Psi_{1/3}\rangle}{\langle \Psi_{1/3}|\Psi_{1/3}\rangle}
$$

$$
= \int d\vec{z}_1 d\vec{z}_2 \rho_{1/3}(\vec{z}_1, \vec{z}_2)\Phi_{\beta m}^*(\vec{z}_1)\Phi_{\beta m}(\vec{z}_2), \qquad (A2)
$$

where $\rho_{1/3}$ is the one-particle reduced density matrix, and $\Phi_{\beta m}$ is the type-I wave function of LLL ($n = 0$). Here, $\rho_{1/3}$ can be described as follows [54]:

$$
\rho_{1/3}(\vec{z}_a, \vec{z}_b)
$$

$$
= \frac{N \int \prod_{i=2}^N d^2\vec{z}_i \Psi_{1/3}^*(\vec{z}_a, \vec{z}_2, \dots \vec{z}_N)\Psi_{1/3}(\vec{z}_b, \vec{z}_2, \dots \vec{z}_N)}{\int \prod_{i=1}^N d^2\vec{z}_i |\Psi_{1/3}|^2}.
$$

$$(A3)$$

In momentum space, the one-particle density matrix can be written as

$$
\rho_{1/3}(\vec{z}_a, \vec{z}_b) = \sum_m n_m^{1/3}\Phi_{\beta m}^*(\vec{z}_a)\Phi_{\beta m}(\vec{z}_b). \qquad (A4)
$$

We choose $\vec{z}_a = z \exp[i(\theta_z + \theta)]$ and $\vec{z}_b = z \exp(i\theta_z)$, which have the same radial distance but differ by an angle θ in the complex coordinate system. Thus,

$$
\rho_{1/3}[\vec{z}_b, \vec{z}_b \exp(-i\theta)] = \sum_m n_m^{1/3}|\Phi_{\beta m}(\vec{z}_b)|^2 \exp(-i\beta m\theta).
$$

$$(A5)$$

Then we consider the above relation as a discrete Fourier transform from momentum-space index m to real-space conjugate θ and set $\vec{z}_b = \vec{z}$. The inverse transformations read

$$
n_m^{1/3}|\Phi_{\beta m}(\vec{z})|^2 = \frac{1}{3N-2}\sum_{j=0}^{3(N-1)} \exp(i\beta m\theta_j)\rho_{1/3}[\vec{z}, \vec{z}\exp(-i\theta_j)],
$$

$$(A6)$$

where $\theta_j = 2\pi j/(3N\beta - 2\beta)$. Then we calculate the occupation number by integrating Eq. (A6) over $\vec{z}$ and get

$$
n_m^{1/3} = \frac{1}{3N-2}\sum_{j=0}^{3(N-1)} \exp(i\beta m\theta_j)\rho_{1/3}(\theta_j), \qquad (A7)
$$

where $\rho_{1/3}(\theta_j) = \int d\vec{z}\rho_{1/3}[\vec{z}, \vec{z}\exp(-i\theta_j)]$. Using Eq. (A3), we have

$$
\rho_{1/3}(\theta_j) = \frac{N \int \prod_{i=1}^N d\vec{z}_i \Psi_{1/3}^*(\vec{z}_1, \vec{z}_2, \dots \vec{z}_N)\Psi_{1/3}[\vec{z}_1 \exp(-i\theta_j), \vec{z}_2, \dots \vec{z}_N]}{\int \prod_{i=1}^N d^2\vec{z}_i |\psi_{1/3}|^2}. \qquad (A8)
$$

Using Eq. (A1), we have

$$
\Psi_{1/3}[\vec{z}_1 \exp(-i\theta_j), \vec{z}_2, \dots] = \Psi_{1/3}(\vec{z}_i)Z_1(\theta_j) \qquad (A9)
$$

$$
Z_a(\theta_j) = \prod_{k\neq a} \frac{\left[\vec{z}_a^{\,\beta}\exp(-i\beta\theta_j) - \vec{z}_k^{\,\beta}\right]^3}{\left(\vec{z}_a^{\,\beta} - \vec{z}_k^{\,\beta}\right)^3}, \qquad (A10)
$$

so we have

$$
\rho_{1/3}(\theta_j) = \frac{N \int \prod_{i=1}^N d^2\vec{z}_i |\Psi_{1/3}|^2 Z_1(\theta_j)}{\int \prod_{i=1}^N d^2\vec{z}_i |\Psi_{1/3}|^2} = N\langle Z_1(\theta_j)\rangle.
$$

$$(A11)$$

Without loss of generality.

$$
\rho_{1/3}(\theta_j) = \sum_{a=1}^N \langle Z_a(\theta_j)\rangle. \qquad (A12)
$$

Using Eqs. (A7), (A10), and (A12), we finally obtain the occupation number $n_m^{1/3}$ from MC simulation.

APPENDIX B: OCCUPATION NUMBER OF $\frac{5}{2}$ MR STATE FROM MC SIMULATION

Similarly, the (unnormalized) wave function corresponding to the $\nu = \frac{5}{2}$ MR state is

$$
\Psi_{5/2} = \mathrm{Pf}\left(\frac{1}{\vec{z}_i^{\,\beta} - \vec{z}_j^{\,\beta}}\right)\prod_{i<j}(\vec{z}_i^{\,\beta} - \vec{z}_j^{\,\beta})^2 \exp\left(-\frac{1}{4}\sum_i z_i^2\right),
$$

$$(B1)$$

where Pf(Z) is the Pfaffian polynomial of matrix Z. For instance, in the $N = 4$ electron system, the matrix Z is equal to

$$
Z = \begin{bmatrix}
0 & \frac{1}{\vec{z}_1^{\,\beta}-\vec{z}_2^{\,\beta}} & \frac{1}{\vec{z}_1^{\,\beta}-\vec{z}_3^{\,\beta}} & \frac{1}{\vec{z}_1^{\,\beta}-\vec{z}_4^{\,\beta}} \\
-\frac{1}{\vec{z}_1^{\,\beta}-\vec{z}_2^{\,\beta}} & 0 & \frac{1}{\vec{z}_2^{\,\beta}-\vec{z}_3^{\,\beta}} & \frac{1}{\vec{z}_2^{\,\beta}-\vec{z}_4^{\,\beta}} \\
-\frac{1}{\vec{z}_1^{\,\beta}-\vec{z}_3^{\,\beta}} & -\frac{1}{\vec{z}_2^{\,\beta}-\vec{z}_3^{\,\beta}} & 0 & \frac{1}{\vec{z}_3^{\,\beta}-\vec{z}_4^{\,\beta}} \\
-\frac{1}{\vec{z}_1^{\,\beta}-\vec{z}_4^{\,\beta}} & -\frac{1}{\vec{z}_2^{\,\beta}-\vec{z}_4^{\,\beta}} & -\frac{1}{\vec{z}_3^{\,\beta}-\vec{z}_4^{\,\beta}} & 0
\end{bmatrix}, \qquad (B2)
$$

and Pf(Z) = $\frac{1}{\vec{z}_1^{\,\beta}-\vec{z}_2^{\,\beta}}\frac{1}{\vec{z}_3^{\,\beta}-\vec{z}_4^{\,\beta}} - \frac{1}{\vec{z}_1^{\,\beta}-\vec{z}_3^{\,\beta}}\frac{1}{\vec{z}_2^{\,\beta}-\vec{z}_4^{\,\beta}} + \frac{1}{\vec{z}_1^{\,\beta}-\vec{z}_4^{\,\beta}}\frac{1}{\vec{z}_2^{\,\beta}-\vec{z}_3^{\,\beta}}$. While Pf($Z$) has a complicated form, its square satisfies $|\mathrm{Pf}(Z)|^2 = |\det[\mathrm{Pf}(Z)]|$. In a similar way, we have

$$
n_m^{5/2} = \frac{1}{2N-2}\sum_{j=0}^{2N-3} \exp(i\beta m\theta_j)\rho_{5/2}(\theta_j), \qquad (B3)
$$

$$
\rho_{5/2}(\theta_j) = \sum_{a=1}^N \langle Z_a(\theta_j)\rangle, \qquad (B4)
$$

$$
Z_a(\theta_j) = \prod_{k\neq a} \frac{\left[\vec{z}_a^{\,\beta}\exp(-i\beta\theta_j) - \vec{z}_k^{\,\beta}\right]^2}{\left(\vec{z}_a^{\,\beta} - \vec{z}_k^{\,\beta}\right)^2}
$$

$$
\times \frac{\mathrm{Pf}\left(Z\{\vec{z}_a^{\,\beta} \to [\vec{z}_a\exp(-i\theta_j)]^\beta\}\right)}{\mathrm{Pf}(Z)}, \qquad (B5)
$$

where $\theta_j = 2\pi j/(2\beta N - 2\beta)$. We implement the Pfaffian polynomial with the help of the algorithm [71].
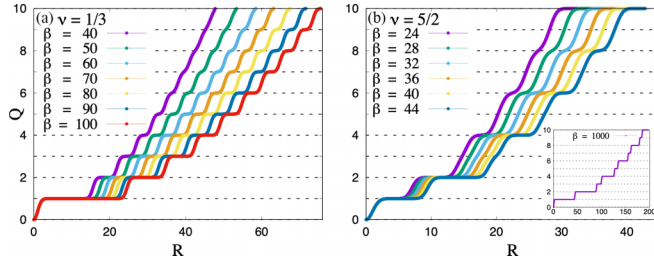
FIG. 12. Charge accumulation Q from Eq. (10) for (a) the $\nu = \frac{1}{3}$ Laughlin state and (b) the $\nu = \frac{5}{2}$ Moore-Read (MR) state with sufficiently big β. The inset in (b) shows the charge-density-wave (CDW) limit for the MR state. Every single charge plateau could be seen.

APPENDIX C: ACCUMULATED ELECTRON CHARGE FOR BIG β CASES

In this Appendix, we supply more numerical results of the accumulated charge for sufficiently big β cases, as shown in Fig. 12.

APPENDIX D: CALCULATION OF OVERLAP BETWEEN DIFFERENT GEOMETRIES

In this Appendix, we give some details on how to calculate the wave-function overlap between different geometries.

In the first step, we need to generate the wave functions of different FQH states with the help of the Jack polynomial

method. Here, we should note that the wave functions in this step are presented in the conformal field theory limit, where the geometry factor of the many-body wave function can be neglected. For example, the $\nu = \frac{1}{3}$ Laughlin state with only two fermions could be constructed as $\Psi_{\nu=1/3}(z_1, z_2) = 1 \times |1001\rangle - 3 \times |0110\rangle$.

The second step follows with adding the corresponding geometry factor to wave functions. Take cone geometry as an example. The single-particle wave function is $\Phi_m(z, \beta) \sim \frac{1}{\sqrt{2^{\beta m}(\beta m)!}} z^{\beta m} \exp(-|z|^2/4)$. The wave function normalization could be executed after multiplying a prefactor which contains the geometry information:

$$
\begin{aligned}
\Psi_{\nu=1/3}^{\beta}(z_1, z_2) \sim {} & 1 \times \sqrt{2^{0\beta}(0\beta)!}\sqrt{2^{3\beta}(3\beta)!} \times |1001\rangle \\
& - 3 \times \sqrt{2^{1\beta}(1\beta)!}\sqrt{2^{2\beta}(2\beta)!} \times |0110\rangle \\
\sim {} & 1 \times \sqrt{(0\beta)!(3\beta)!} \times |1001\rangle \\
& - 3 \times \sqrt{(1\beta)!(2\beta)!} \times |0110\rangle.
\end{aligned}
$$

Thus, the FQH state wave function $\Psi_{\text{cone}}(\beta)$ on a cone could be obtained. In a similar way, one gets the wave function $\Psi_{\text{cylinder}}(L_x)$ on a cylinder with parameter L_x.

The third step follows with calculating the inner product between $\Psi_{\text{cone}}(\beta)$ and $\Psi_{\text{cylinder}(L_x)}$ straightforwardly. Finally, one gets the overlap between different geometries $\langle \Psi_{\text{cone}}(\beta)|\Psi_{\text{cylinder}}(L_x)\rangle$.

[1] D. C. Tsui, H. L. Stormer, and A. C. Gossard, Phys. Rev. Lett. **48**, 1559 (1982).

[2] R. B. Laughlin, Phys. Rev. Lett. **50**, 1395 (1983).

[3] R. Willett, J. P. Eisenstein, H. L. Störmer, D. C. Tsui, A. C. Gossard, and J. H. English, Phys. Rev. Lett. **59**, 1776 (1987).

[4] G. Moore and N. Read, Nucl. Phys. B **360**, 362 (1991).

[5] J. E. Avron, R. Seiler, and P. G. Zograf, Phys. Rev. Lett. **75**, 697 (1995).

[6] P. Lèvay, J. Math. Phys. **36**, 2792 (1995).

[7] D. X. Qu, X. Che, X. Kou, L. Pan, J. Crowhurst, M. R. Armstrong, J. Dubois, K. L. Wang, and G. F. Chapline, Phys. Rev. B **97**, 045308 (2018).

[8] B. Bradlyn and N. Read, Phys. Rev. B **91**, 165306 (2015).

[9] T. Can, M. Laskin, and P. Wiegmann, Phys. Rev. Lett. **113**, 046803 (2014).

[10] A. G. Abanov and A. Gromov, Phys. Rev. B **90**, 014435 (2014).

[11] F. D. M. Haldane, Phys. Rev. Lett. **107**, 116801 (2011).

[12] Y. Park and F. D. M. Haldane, Phys. Rev. B **90**, 045123 (2014).

[13] X. G. Wen and A. Zee, Phys. Rev. Lett. **69**, 953 (1992).

[14] T. Can, Y. H. Chiu, M. Laskin, and P. Wiegmann, Phys. Rev. Lett. **117**, 266803 (2016).

[15] R. R. Biswas and D. T. Son, Proc. Natl. Acad. Sci. USA **113**, 8636 (2016).

[16] Y.-H. Wu, H.-H. Tu, and G. J. Sreejith, Phys. Rev. A **96**, 033622 (2017).

[17] N. Gemelke, E. Sarajlic, and S. Chu, arXiv:1007.2677.

[18] M. Aidelsburger, M. Atala, M. Lohse, J. T. Barreiro, B. Paredes, and I. Bloch, Phys. Rev. Lett. **111**, 185301 (2013).

[19] C. J. Kennedy, W. C. Burton, W. C. Chung, and W. Ketterle, Nat. Phys. **11**, 859 (2015).

[20] H. Miyake, G. A. Siviloglou, C. J. Kennedy, W. C. Burton, and W. Ketterle, Phys. Rev. Lett. **111**, 185302 (2013).

[21] M. Aidelsburger, M. Lohse, C. Schweizer, M. Atala, J. T. Barreiro, S. Nascimbène, N. Cooper, I. Bloch, and N. Goldman, Nat. Phys. **11**, 162 (2015).

[22] E. Doko, A. L. Subasi, and M. Iskin, Phys. Rev. A **93**, 033640 (2016).

[23] Y. J. Lin, R. L. Compton, K. Jimenez-Garcia, J. V. Porto, and I. B. Spielman, Nature (London) **462**, 628 (2009).

[24] G. Juzeliūnas and P. Öhberg, Phys. Rev. Lett. **93**, 033602 (2004).

[25] D. Peter, A. Griesmaier, T. Pfau, and H. P. Büchler, Phys. Rev. Lett. **110**, 145303 (2013).

[26] M. Lu, S. H. Youn, and B. L. Lev, Phys. Rev. Lett. **104**, 063001 (2010).

[27] K.-K. Ni, S. Ospelkaus, M. H. G. de Miranda, A. Pe'er, B. Neyenhuis, J. J. Zirbel, S. Kotochigova, P. S. Julienne, D. S. Jin, and J. Ye, Science **322**, 231 (2008).

[28] N. R. Cooper, Adv. Phys. **57**, 539 (2008).

[29] A. L. Fetter, Rev. Mod. Phys. **81**, 647 (2009).

[30] M. A. Baranov, K. Osterloh, and M. Lewenstein, Phys. Rev. Lett. **94**, 070404 (2005).

[31] K. Osterloh, N. Barberán, and M. Lewenstein, Phys. Rev. Lett. **99**, 160403 (2007).

[32] M. A. Baranov, H. Fehrmann, and M. Lewenstein, Phys. Rev. Lett. **100**, 200402 (2008).

[33] R. Z. Qiu, S. P. Kou, Z.-X. Hu, X. Wan, and S. Yi, Phys. Rev. A **83**, 063633 (2011).

[34] Z.-X. Hu, Q. Li, L. P. Yang, W. Q. Yang, N. Jiang, R. Z. Qiu, and B. Yang, Phys. Rev. B **97**, 035140 (2018).

[35] S. Mittal, S. Ganeshan, J. Fan, A. Vaezi, and M. Hafezi, Nat. Photon. **10**, 180 (2016).

[36] J. Otterbach, J. Ruseckas, R. G. Unanyan, G. Juzeliūnas, and M. Fleischhauer, Phys. Rev. Lett. **104**, 033903 (2010).

[37] G. Juzeliūnas, P. Öhberg, J. Ruseckas, and A. Klein, Phys. Rev. A **71**, 053614 (2005).

[38] N. Schine, A. Ryou, A. Gromov, A. Sommer, and J. Simon, Nature (London) **534**, 671 (2016).

[39] N. Schine, M. Chalupnik, T. Can, A. Gromov, and J. Simon, Nature (London) **565**, 173 (2019).

[40] L. W. Clark, N. Schine, C. Baum, N. Jia, and J. Simon, Nature (London) **582**, 41 (2020).

[41] W. Zhu, D. N. Sheng, and K. Yang, Phys. Rev. Lett. **125**, 146802 (2020).

[42] K. Yang, Phys. Rev. B **96**, 241305(R) (2017).

[43] U. Khanna, M. Goldstein, and Y. Gefen, Phys. Rev. B **103**, L121302 (2021).

[44] U. Khanna, M. Goldstein, and Y. Gefen, Phys. Rev. Lett. **129**, 146801 (2022).

[45] G. Y. Cho, Y. You, and E. Fradkin, Phys. Rev. B **90**, 115139 (2014).

[46] M. J. Bueno, C. Furtado, and A. M. de M. Carvalho, Eur. Phys. J. B **85**, 53 (2012).

[47] F. D. M. Haldane, Phys. Rev. Lett. **51**, 605 (1983).

[48] B. A. Bernevig and F. D. M. Haldane, Phys. Rev. Lett. **100**, 246802 (2008).

[49] B. A. Bernevig and F. D. M. Haldane, Phys. Rev. Lett. **101**, 246806 (2008).

[50] B. A. Bernevig and N. Regnault, Phys. Rev. Lett. **103**, 206801 (2009).

[51] T. Can, M. Laskin, and P. Wiegmann, Ann. Phys. **362**, 752 (2015).

[52] R. Morf and B. I. Halperin, Phys. Rev. B **33**, 2221 (1986).

[53] S. Mitra and A. H. MacDonald, Phys. Rev. B **48**, 2005 (1993).

[54] J. K. Jain, *Composite Fermions* (Cambridge University Press, Cambridge, 2007).

[55] E. H. Rezayi and F. D. M. Haldane, Phys. Rev. B **50**, 17199 (1994).

[56] A. Seidel, H. Fu, D.-H. Lee, J. M. Leinaas, and J. Moore, Phys. Rev. Lett. **95**, 266405 (2005).

[57] E. J. Bergholtz and A. Karlhede, J. Stat. Mech. (2006) L04001.

[58] R. Tao and D. J. Thouless, Phys. Rev. B **28**, 1142 (1983).

[59] O. Ciftja and C. Wexler, Phys. Rev. B **67**, 075304 (2003).

[60] H. Li and F. D. M. Haldane, Phys. Rev. Lett. **101**, 010504 (2008).

[61] M. Haque, O. Zozulya, and K. Schoutens, Phys. Rev. Lett. **98**, 060401 (2007).

[62] O. S. Zozulya, M. Haque, K. Schoutens, and E. H. Rezayi, Phys. Rev. B **76**, 125310 (2007).

[63] J. Dubail, N. Read, and E. H. Rezayi, Phys. Rev. B **85**, 115321 (2012).

[64] A. Sterdyniak, A. Chandran, N. Regnault, B. A. Bernevig, and P. Bonderson, Phys. Rev. B **85**, 125308 (2012).

[65] A. Hamma, R. Ionicioiu, and P. Zanardi, Phys. Lett. A **337**, 22 (2005).

[66] A. Kitaev and J. Preskill, Phys. Rev. Lett. **96**, 110404 (2006).

[67] M. Levin and X. G. Wen, Phys. Rev. Lett. **96**, 110405 (2006).

[68] A. M. Chang, L. N. Pfeiffer, and K. W. West, Phys. Rev. Lett. **77**, 2538 (1996).

[69] X. G. Wen, Int. J. Mod. Phys. B **06**, 1711 (1992).

[70] X. G. Wen, Adv. Phys. **44**, 405 (1995).

[71] M. Wimmer, ACM Trans. Math. Software **38**, 1 (2012).